Food Hydrocolloids 120 (2021) 106916

Contents lists available at ScienceDirect

Food Hydrocolloids

journal homepage: www.elsevier.com/locate/foodhyd

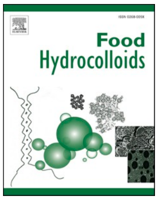

Protein gel shrinkage during solvent exchange: Quantification of gel compaction, mass transfer and compressive strength

Martin P. Dirauf[a], Anja Hajnal[b], Pavel Gurikov[b], Andreas S. Braeuer[a,*]

[a] Institute of Thermal-, Environmental-, and Resources' Process Engineering (ITUN), Technische Universität Bergakademie Freiberg (TUBAF), Leipziger Strasse 28, 09599, Freiberg, Germany
[b] Laboratory for Development and Modelling of Novel Nanoporous Materials, Hamburg University of Technology, Eissendorfer Strasse 38, 21073, Hamburg, Germany

ARTICLE INFO

Keywords:
Protein gels
Whey protein isolate
Solvent exchange
Shrinkage
1-D Raman spectroscopy

ABSTRACT

In this work, we experimentally investigate into one step solvent exchange of cylindrical shaped whey protein isolate (WPI) gels, where the pore fluid water inside the pores is replaced by ethanol. Solvent exchange has three major impacts on macroscopic gel properties, leading to an increase in compressive strength, shrinkage of the gel cylinders diameter and consequently a change in the spatial protein distribution. 1D-Raman spectroscopy was employed for *in-situ* investigation of pore fluid composition and protein density distribution, together with a conventional camera to track the diameter change of the gel during solvent exchange. Compressive strength of the gel cylinders is measured *ex-situ* using a universal testing machine. For gels with three different protein concentrations, we report comparable shrinkage of the diameter to about 85% of the initial size, with most shrinkage taking place during the first stages of solvent exchange, when ethanol is detected in the outermost layers only. Further shrinkage is prevented by a sharp increase in mechanical stiffness of the gels. Solvent exchange leads to an inhomogeneous protein density distribution for most gels, with a compaction towards the radial center. We showed a complex interaction of solvent exchange kinetics and pore fluid dependent stiffness of the gel matrix controls the final size and density distribution of the gel.

1. Introduction

Biopolymer aerogels (bio-aerogels for short) are open structured mesoporous solids that feature ultra-low density, high porosity and specific surface area, low heat conductivity, biocompatibility and biodegradability (Fricke & Tillotson, 1997; Soorbaghi et al., 2019). While the pores of a bio-aerogel are filled with air, its solid backbone is made of a cross-linked biopolymer. Precursors for biopolymer gels are mostly polysaccharides like alginate (Gurikov, Raman, Weinrich, Fricke, & Smirnova, 2015), starch (Zhu, 2019), pectin (Groult & Budtova, 2018) or proteins such as egg white (Selmer, Kleemann, Kulozik, Heinrich, & Smirnova, 2015), whey (Betz, García-González, Subrahmanyam, Smirnova, & Kulozik, 2012), casein (Kleemann, Selmer, Smirnova, & Kulozik, 2018) or silk (Marin, Mallepally, & McHugh, 2014). The combination of high porosity and large surface area together with biocompatibility make bio-aerogels ideal materials in food and life science applications as porous carrier matrices for the defined or efficient release of pharmaceutically active compounds or food supplements (El-Naggar, Othman, Allam, & Morsy, 2020; Stergar & Maver, 2016).

Due to the natural origin of the precursors, the gelation step is usually carried out in an aqueous environment (Maleki et al., 2016), resulting in a biopolymer hydrogel. The pores of such hydrogels are filled with water. Due to the fragile porous structure, biopolymer hydrogels cannot be dried to aerogels using simple ambient-pressure drying methods. Capillary forces would cause a pore collapse and would destroy the desired open porous structure of the gel. The emergence of capillary forces is avoided by removing the pore liquid in a single-fluid phase process. For this purpose the pore-liquid water is first exchanged by an organic solvent which at moderate pressures and mild temperatures features complete miscibility with the drying agent carbon dioxide (CO_2) (García-González, Camino-Rey, Alnaief, Zetzl & Smirnova, 2012). Though the solvent exchange only prepares the gel for the final drying step, the solvent exchange usually remains the greatest cause for severe shrinkage during bio-aerogels synthesis (Gurikov, S. P., Griffin, Steiner, & Smirnova, 2019; Mehling, Smirnova, Guenther, & Neubert, 2009; Quignard, Valentin, & Di Renzo, 2008). As an example, a volumetric shrinkage of more than 90 % has been reported when alginate hydrogels were exposed to pure ethanol in a single-stage solvent

---

* Corresponding author.
E-mail address: Andreas.Braeuer@tu-freiberg.de (A.S. Braeuer).

https://doi.org/10.1016/j.foodhyd.2021.106916
Received 10 December 2020; Received in revised form 20 May 2021; Accepted 23 May 2021
Available online 31 May 2021

exchange process. This is mainly attributed to changing the solvent-matrix interactions when the pore-liquid gets less-polar during solvent exchange (Subrahmanyam, Gurikov, Dieringer, Sun, & Smirnova, 2015). For most types of biopolymer hydrogels, shrinkage can be decreased decisively when the composition gradient of the water/-organic solvent mixture inside the gel is small. This is usually achieved by a stepwise gradual solvent exchange (García-González et al., 2011).

During solvent exchange the shrinkage of biopolymer hydrogels is countered by the intrinsic stiffness of the solid backbone of the gel: Gels with a larger fraction of matrix material are reported to shrink less during solvent exchange (Gurikov, RGriffin, Steiner, & Smirnova, 2019).

Gelation of aqueous protein solutions can be carried out via various routes, among them acid- (Chen, Dickinson, & Edwards, 1999), salt- (Hongsprabhas & Barbut, 1997), ethanol- (Uzun, Kim, Leal, & Padua, 2016) and heat (Betz et al., 2012)- induced gelation. Main building blocks of whey proteins are β-lactoglobulin and α-lactoglobulin. While β-lactoglobulin has a free sulfhydryl group inside its folded native structure, α-lactalbumin has no free sulfhydryl group (Wolz & Kulozik, 2015). Gelation of protein solutions leads to the denaturation of the native folding which modifies the protein conformation, especially in the secondary structure (Van Kleef, 1986). For heat- and ethanol-induced gelation, a shift of the secondary structure from α-helices to β-sheets has been reported (Nonaka, Li-Chan, & Nakai, 1993; Uzun et al., 2016). This partial unfolding of denatured proteins results in the exposure of the free sulfhydryl group of the β-lactoglobulin and hydrophobic residues. Further intermolecular covalent disulfide interactions and noncovalent interactions cause protein aggregation and gel network formation (Wolz & Kulozik, 2015). The gelation relevant interactions and structural characteristics are dependent on the nature of the pore fluid inside the gel and influence the behavior of the gel during solvent exchange.

In this work, we give insights into the solvent exchange and shrinkage of whey protein isolate hydrogels when exposed to pure ethanol using a combination of three different techniques.

The solvent exchange and the gel matrix material shrinkage inside the gels was analyzed using one-dimensional Raman spectroscopy. Photography was used for monitoring the shrinkage of the gel monolith. Lastly, as stiffness of the gel matrix resists to the tendency of the gel matrix to contract during solvent exchange, the Young's modulus of the gels at certain instants during solvent exchange is measured.

Spatially resolved Raman spectroscopy was previously used for the observation of concentration profiles inside a hydrogel during solvent exchange (Naddaf & Bart, 2011). Furthermore, the use of Raman spectroscopy has also been reported to measure the local polymer density distribution in biopolymer gels: Heinemann et al. investigated into the spatial distribution of alginate in spherical alginate beads produced by solvent-based gelation (Matthias Heinemann et al., 2004). Based on the preliminary work using Raman spectroscopy for tracking solvent exchange on the one hand and shedding light on the spatial density distribution of the matrix material in biopolymer gels on the other hand, in this work Raman spectroscopy was used to directly observe how composition gradients of the pore liquid during solvent exchange affect local changes in the spatial density distribution of the matrix material of the WPI gel. In order to also investigate into the relationship between solvent gradients, shrinkage and mechanical stiffness, next to Raman spectroscopy, the gel diameter and the Young's modulus of the gel are measured.

2. Materials and methods

2.1. Materials

Whey protein isolate (WPI; *Pure Whey Isolate 97*) with a protein content of 97.6 *wt*% was purchased from Bulk Powders (Colchester, England). Deionized water was used from a stationary reverse osmosis system. Ethanol (EtOH; *absolute for analysis*) and sodium hydroxide were purchased from VWR international. All Chemicals were used without further purification.

2.2. Preparation of the WPI hydrogel monoliths and solvent exchange

Protein hydrogels were synthesized from rehydrated whey protein isolate solution using heat-set gelation according to a common protocol (Betz et al., 2012). The pH of deionized water was set to $pH = 9$ by adding of 0.1 *M* sodium hydroxide. Then, WPI powder was weighed, mixed with the previously prepared water and vigorously shaken till all solids were dissolved. The result is a transparent WPI solution with a light yellowish color. The WPI solution is stored at 277 *K* overnight to allow for rehydration of the proteins. The WPI solution is then poured into disposable syringes ($V_{syringe} = 3\ ml$) which have their tip and upper part removed. The inner diameter of the syringe cylinder is 10 *mm* and defines the outer diameter of the later produced gel. For the prevention of vapor-loss during gelation, the open end of each syringe is covered with aluminum foil. The covered syringes are placed into a water bath at room temperature which is then heated to 353 *K* and kept at this temperature for 15 *min*. The WPI solution inside the syringes adopts the temperature of the water bath and turns into a gel. The hydrogel-containing syringes are taken out of the water bath. The gels remain inside the syringes for at least 30 *min* and accommodate to room temperature. The resulting hydrogels have a diameter of 10 *mm* and a height of 20 *mm*, which corresponds to a volume of 1.5 *ml*. The hydrogel cylinders are casted out of the syringes by moving the die of the syringe. Once removed from the syringe cylinder, the hydrogel monoliths are immediately subjected to solvent exchange.

For solvent exchange the WPI hydrogel is placed in a glass-cuvette that contains approximately 80 *ml* of ethanol at room temperature. When positioned inside the cuvette, the gel is completely surrounded and covered by ethanol.

2.3. One-dimensional Raman spectroscopy

A comprehensive description of the one-dimensional Raman spectroscopy setup and its working principle can be found elsewhere (Quiño et al., 2016). The measurement setup employed in this study is shown in Fig. 1 and described in detail below.

In order to minimize the unwanted fluorescence interference from the gel sample, a diode laser with an emission wavelength of 785 *nm* and a maximum power of 2.5 *W* is used (*Sacher Lasertechnik TEC-420-0785-2500*). The laser is operated at 2.2 *W*. The laser beam polarization is turned to perpendicular (vertical) using a half wave plate (HWP). A flip mirror (M2) directs the laser beam to a beam dump whenever no Raman spectra are recorded and lets the laser pass through to the gel in the case of a measurement event. The laser beam is widened using a Galilean telescope composed of lens 1 and lens 2 by a factor of 5 and then focused through the gel cylinder by a third lens (L3). The laser beam waist is imaged (lens 4 and 5) under 90° onto the horizontally aligned entrance slit of an imaging spectrograph (*Andor Shamrock 303i*). A long-pass filter (LPF) with a cut-off wavelength at 822 *nm* discriminates against elastically scattered light. The remaining light is spectrally dispersed by a 300 l/mm reflection grating inside the spectrograph and detected with a front illuminated charge coupled device (CCD)-detector *(CCD1, Andor Newton)* with a pixel-resolution of 1024 pixels along the spectral dimension and 255 pixels along the spatial dimension. A front illuminated camera was chosen despite its much weaker quantum efficiency in the VIS/NIR wavelength region when compared to a back illuminated model. The reason is that the back illuminated model showed severe spectral etaloning behavior in the observed wavelength region. The two lenses in the detection pathway (L4 & L5) lead to a magnification of -0.4. Thereby 16 *mm* of the laser beam inside the gel are imaged onto the 6.4 *mm* wide (spatial dimension) chip of the camera “CCD1”. The 255 pixels along the spatial dimension are binned in groups of 15 pixels resulting in $(255/15) = 17$ spatially resolvable increments along the

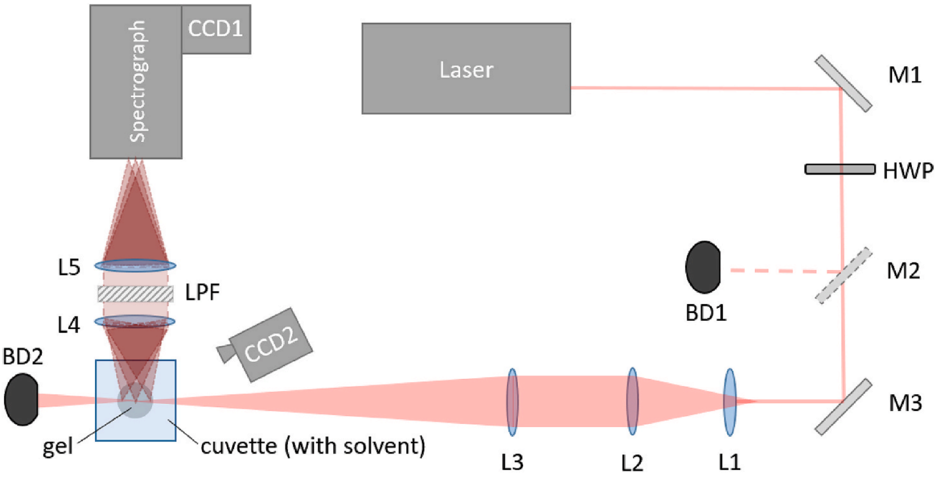

Fig. 1. Sketch of the Raman setup. The direction of the laser beam can be adjusted by two mirrors (M1, M3). The flip mirror (M2) enables redirecting the laser beam away from the probe. The polarization of the beam is directed to perpendicular (vertical) with a half wave plate (HWP). The beam is widened by a Galilean telescope consisting of the lenses L1 ($f = -30\ mm$) and L2 ($f = 150\ mm$) and then focused by L3 ($f = 500\ mm$) through the gel sample situated inside the ethanol-filled cuvette. Elastically and inelastically scattered light is collected by L4 ($f = 250\ mm$) and imaged on the entrance slit of the spectrograph by L5 ($f = 100\ mm$). Elastically scattered light is suppressed in the detection path using a long pass filter (LPF, cut off $= 822\ nm$).

laser beam, where each increment corresponds to $(16mm\,/17increments) = 0.94\ mm/increment$. During each measurement event, Raman signals were cumulated on the CCD chip of CCD1 over a period of $25\ s$. This signal integration time represents the temporal resolution of one measurement event. Measurements were executed in time intervals of $15\ min$, which corresponds to a measurement repetition rate of $4/h$.

2.4. *Photographic analysis of shrinkage*

The evolution of the diameter of the gel during solvent exchange is monitored by photography with a CCD-camera *(Allied Vision Guppy Pro, CCD2 in* Fig. 1*)*. Here again, a photo is taken each $15\ min$ and evaluated by an edge detection script in order to quantify the diameter of the upright standing gel cylinder at half height of the gel. The consideration of the gel diameter instead of the gel volume implies a straightforward correlation with the one-dimensional measurement results originating from the Raman measurements.

The gel diameters were calculated from the photos using a self-engineered MATLAB script. The Hough transformation was applied to detect all vertical lines ($\pm 1^\circ$) that were revealed by the Canny edge detection of before binarized photos. The distance between the two nearly parallel vertical lines represents the diameter of the gel at half height of the upright standing gel.

2.5. *Compressive strength measurements*

18 WPI-hydrogels of cylindrical shape from the same production were simultaneously put in a bottle containing 800 ml ethanol. All gels were completely covered and surrounded by ethanol. At each measurement point in time, three gels were taken out of the bottle. Their compressive strength was measured immediately and then probed gels were discarded. Thus, the compressive strength was measured for 6 different instants in time ($0\ min$, $45\ min$, $90\ min$, $180\ min$, $360\ min$, $705\ min$) as a triplicate. Stress-strain curves for the compression of the upright standing gels were recorded on a universal testing machine *(Hegenwald & Peschke Inspekt Mini* 3 kN*)*. The test cycle consisted of a compression path of $4\ mm$ and the relaxation to the starting point. Movement speed of the compression die was set to $1\ mm\,s^{-1}$. For calculation of the resulting pressure from the recorded force, the initial diameter of the hydrogel ($d = 10\ mm$) was used. The diameter of the die of the testing machine was much larger than the gel itself. Strain ε was calculated from the deformation of the gel and the initial height ($h = 2\ cm$). The Young's modulus was derived from the linear initial slopes ($\varepsilon_{max} = 0.02$) of the stress-strain curves.

3. Results and discussion

3.1. *Raman spectra*

Fig. 2 a shows the WPI gel standing upright in the ethanol cuvette during solvent exchange. The gel is completely surrounded and covered by ethanol. The laser passes the cuvette and the gel. Due to the intensive elastic light scattering from the nanostructured gel matrix and the comparable negligible elastic light scattering from liquid ethanol, the laser is visible as reddish line only inside the gel. The sketched red lines indicate the path of the laser outside of the gel.

Fig. 2 b shows an example image acquired on the chip of CCD1 within the signal integration time of one measurement event of $25\ s$. Each of the 17 pixel columns represents one measurement location along the laser beam transiting the gel, with the very left column (pixel column 1) showing the Raman spectrum originating from the matter at the left boundary of the probe volume. The greenish dashed lines link the pixel column position in Fig. 2 b with the real measurement location in Fig. 2 a. The very left and the very right measurement positions are situated outside the gel. Pixel column 9 for example represents the Raman spectrum of the matter in the center of the gel cylinder. Each pixel column contains 1024 pixels along the spectral axis. The pixel (spectral) vertical axis on the left in Fig. 2 b is converted into the Raman shift on the right vertical axis. Summarizing, during one measurement event of $25\ s$ a total of 17 Raman spectra are recorded simultaneously with each Raman spectrum corresponding to a different location along the $16\ mm$ long one-dimensional probe volume. These 17 Raman spectra are shown in Fig. 2 c. Signals with Raman shifts ν_R from 1543 to 1711 cm^{-1} are assigned to the protein, from 2662 to 2757 cm^{-1} to ethanol (EtOH) and from 3316 to 3549 cm^{-1} to water (H_2O). The intensities of the corresponding signals $I_{Protein}$, I_{EtOH} and I_{H2O} are the integral of the spectrum between those integration boundaries. After a calibration of the Raman spectra in mixtures of defined composition, the fraction of each compound (protein, ethanol and water) in a mixture of unknown composition can be derived from the intensity ratios. A detailed description of spectra processing, calibration routine and the derivation of the weight fractions is presented in appendix A.

From Fig. 2 b and c, qualitative information about the gel position can already be extracted without calibration: Raman signal of the protein is only observable for pixel columns 5 to 14 which correspond to measurement locations $z = 4.7\ mm$ to $z = 13{,}18\ mm$. At the same measurement locations, no Raman signal of ethanol is observable, as these measurements were made at the very beginning of the solvent exchange when quasi no ethanol can be found inside the gel.

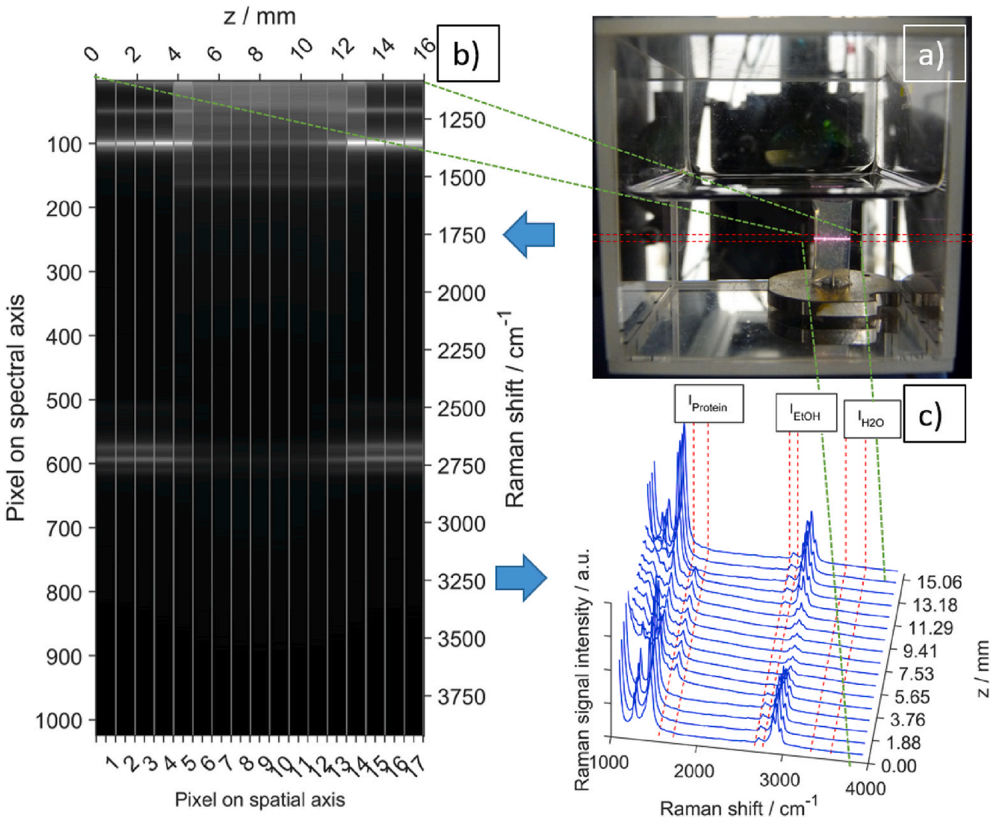

Fig. 2. Illustration of the detection of the spatially resolved Raman signals inside and outside the WPI gel during solvent exchange: The laser transits the center of the gel (a). The generated Raman spectra are recorded along the beam waist spatially resolved on the detector (CCD1) with its 17 super pixels in the spatial and 1024 pixel in spectral dimension (b) resulting in 17 spectra from 17 positions along the laser beam propagation direction (c).

3.2. Composition profiles

It is assumed that after complete gelation the liquid phase outside and inside the gel is composed of water and/or ethanol only. The composition of this binary liquid phase is quantified as ethanol weight fraction w_{EtOH}. As an example, Fig. 3 a shows the temporal evolution of the measured composition profile of the liquid along the one-dimensional probe volume for a WPI hydrogel gelled from a 20 *wt*% WPI aqueous solution. Fig. 3 b shows the composition profiles extracted for six instants (0 *min*, 45 *min*, 90 *min*, 180 *min*, 360 *min*, 705 *min*). At $t = 0$ *min* the hydrogel was exposed to pure ethanol. Therefore at $t = 0$ *min* ethanol cannot be found in the center of the gel but outside the gel. With time, the composition profiles inside the gel degrade towards larger ethanol fractions, until at the end of solvent exchange ($t = 705$ *min*) the liquid inside the gel is quasi pure ethanol.

The red circles in Fig. 3 a indicate the position of the edges of the gel

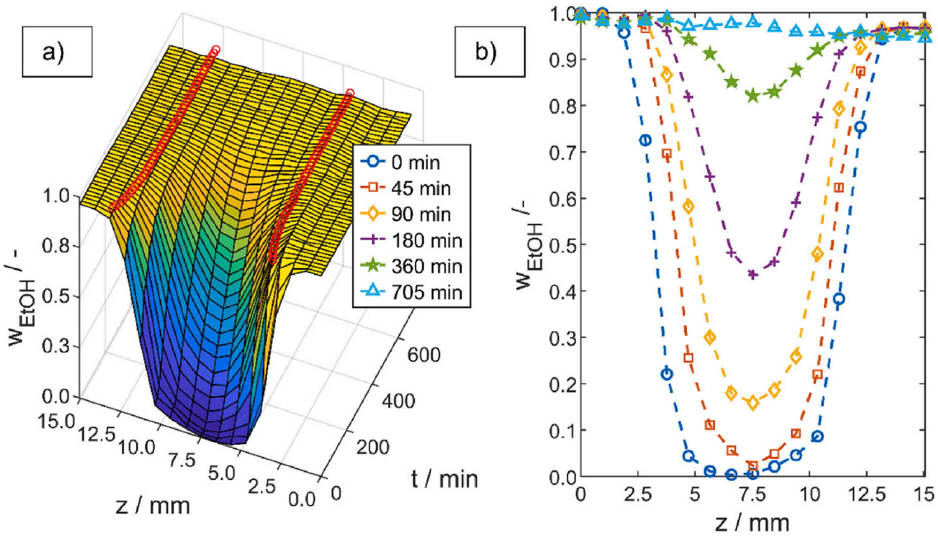

Fig. 3. Evolution of the composition profile w_{EtOH} for a 20 *wt*% WPI hydrogel in pure EtOH (a) and some composition profiles extracted for 6 different instances of time (b). Red circles in (a) show boundaries of the gel as determined by CCD2 (photography). (For interpretation of the references to color in this figure legend, the reader is referred to the Web version of this article.)

as acquired by photography at that height of the upright standing gel cylinder, where the laser penetrates it. Thus, the distance between two red circles defines the diameter of the gel. During solvent exchange the diameter of the gel reduces from originally 10 *mm*, to about 8.4 *mm*. The shrinkage rate (change of diameter during a certain time interval; $\frac{\Delta d}{\Delta t}$) is largest at the beginning of solvent exchange and then steadily decreases. More than 50 % of the diameter shrinkage occurs during the first 90 *min* and no observable shrinkage occurs after 300 *min*. When comparing the development of the shrinkage to the development of the composition profiles, it is worth underlining that during the first 90 *min*, when more than 50% of the shrinkage has already taken place, the core region of the gel is still rich in water, while the boundary regions are already rich in ethanol. Nonetheless, at 90 *min* already 17 *wt*% ethanol is detected in the center of the gel. After about 300 *min*, the diameter of the gel remains constant, even though the composition profiles show that the fraction of ethanol in the center of the gel is still smaller than 50 *wt*%. A detailed depiction of the temporal evolution of the gel diameter can be found in Fig. 8.

For the description of the changing density of the protein matrix during solvent exchange we here define the protein loading

$$L_{protein} = \frac{m_{Protein}}{V_{pore}} = \frac{m_{Protein}}{V_{pore\ liquid}} = \frac{m_{Protein}}{v_{pore\ liquid}\cdot m_{liquid}} = \frac{w_{Protein}}{v_{pore\ liquid}\cdot w_{liquid}} \qquad (1)$$

as the ratio of the mass of the protein $m_{Protein}$ and the pore volume of the gel V_{pore}, excluding explicitly the volume the protein occupies inside the gel. The protein loading can be quantified from the detected Raman spectra, assuming that the entire pore volume is occupied by pore liquid ($V_{pore} = V_{pore\ liquid}$). The specific volume (the reciprocal density) $v_{pore\ liquid}$ of binary ethanol/water mixtures is taken from literature (Grolier & Wilhelm, 1981) as a function of the mixture composition. The protein and liquid weight fractions are derived from the Raman spectra. The introduction of the protein loading has the advantage of getting a measure of the density distribution of the protein matrix without having to know the skeletal density of the protein in varying pore liquid compositions.

Fig. 4 shows the corresponding evolution of the protein loading. At $t = 0$ *min*, the protein is distributed homogeneously in the middle of the sample with a larger loading at the edges. The latter may be caused by water transport in the radial direction due to temperature gradients which are emerging at the gelation step owing to limited heat transfer through the gelation mold and heat absorption for the protein denaturation. From $t = 0$ *min* to approximately $t = 60$ *min*, the protein matrix material on the edges of the gel shows both, a shrinkage and an increase in protein loading. Therefore, the initial shrinkage of the gel is mainly caused by a compaction of the gel matrix at the edges. For $t > 60$ *min* to $t = 705$ *min* this protein loading distribution practically undergoes an inversion with the dense protein matrix area being located now at the center of the gel.

3.3. Gel shrinkage and compressive strength

When handling the gel before and after solvent exchange, a rather obvious observation about its mechanical strength can be made: Whereas the hydrogel is flexible and elastic to a certain extent, the alcogel (gel with ethanol inside the pores) is rigid.

In order to quantify these observations and possibly relate them to the evolution of shrinkage, the Young's modulus of compression of the gels after different times of solvent exchange was measured in a universal testing machine.

In Fig. 5 the compressive strength of the gels, which were subject to solvent exchange for various times, are plotted as a function of the axial

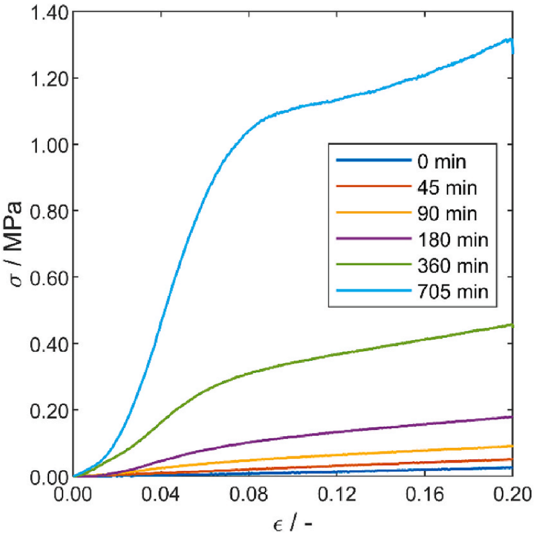

Fig. 5. Stress-Strain curves of 20 *wt*% WPI gels during single-stage solvent exchange with pure ethanol.

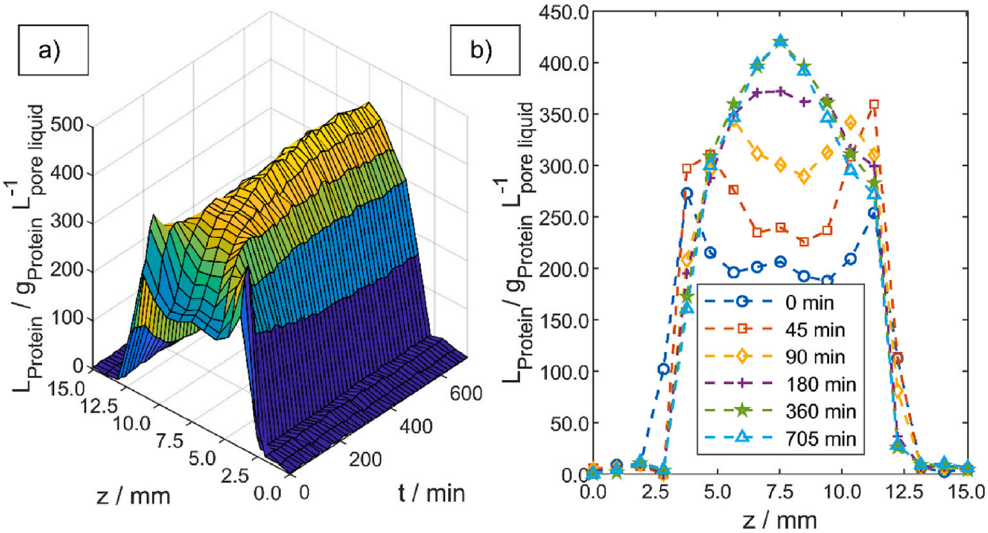

Fig. 4. Evolution of the protein loading distribution of the protein matrix for a 20 *wt*% WPI hydrogel in pure EtOH (a) and some composition profiles extracted for 6 different instants of time (b).

compression ε. The axial compression is the deformation of the gel relative to its original axial dimension. An $\varepsilon = 0.2$ thus corresponds to a deformation of 4 *mm*. The hydrogel before solvent exchange ($t = 0$ *min*) shows the smallest compressive strength and the alcogel ($t = 705$ *min*) the largest. With increasing time of exposure to pure ethanol, the compressive strength of the gels increases.

The Young's modulus of compression of the WPI gels is extracted from the approximately linear initial slope of the compressive strength curves ($\varepsilon < 0.02$) and shown in Fig. 6. The error bars represent the standard deviation of the triplicates of the experiments with 18 different gels. The Young's modulus of compression is 0.13 *MPa* for the hydrogel before solvent exchange and during the first 90 *min* of solvent exchange more than triples its value. After solvent exchange, the Young's modulus of the gel has increased by more than a factor of 30. The increasing deformation resistance likely counteracts the compaction of the protein matrix and most probably is responsible for the rather small shrinkage of WPI gels in a single-stage solvent exchange process with ethanol. It has been proposed that changes in the protein structure and consequently the mechanical strength of protein gels due to alcohols include several mechanisms including increased intermolecular hydrogen bonding, reduction in the hydrophobicity of the protein chain and a selective solvation of amino acid residues (Buck, 1998).

Similarly, mechanical strength measurements would also be possible for biopolymer hydrogels which show low to moderate shrinkage during one step solvent exchange such as chitin, chitosan, starch, cellulose or pectin. For alginate and guar galactomannan gels, volumetric shrinkage of over 90 % was reported for a one step solvent exchange in ethanol and other solvents (Subrahmanyam et al., 2015). For such hydrogel/solvent systems that undergo large volume reduction, mechanical stiffness could be investigated during a stepwise solvent exchange procedure, which will be a subject of future work.

3.4. *Influence of gel matrix density on solvent exchange behavior*

It is widely accepted in literature that biopolymer hydrogels with a higher matrix density tend to resist the compaction of their matrix during solvent exchange far better and thereby exhibit smaller shrinkage than the gel of the same nature, but smaller matrix density (Gurikov et al., 2019). In order to confirm this for WPI gels, additional gels with protein fractions of 15 and 22.5 *wt*% in the original aqueous protein solution were subjected to solvent exchange in pure ethanol. Fig. 7 (top row) shows the composition profiles of the binary water/ethanol mixture for solvent exchange times of 0, 90, 360 *and* 705 *min*. With advancing time, the composition profiles increasingly deviate from each other until all water has been replaced by ethanol at 705 *min*. Gels with larger protein density need more time for solvent exchange. This is expected as the equilibrium time is a function of the polymer volume fraction. Fig. 7 (bottom row) shows the evolution of the protein loading for the three different gels for the same 4 different instants of time. At the beginning of solvent exchange ($t = 0$ *min*) the protein is rather homogeneously distributed along the probe volume. With the progression of solvent exchange, shrinkage of the gels and the resulting compaction of the protein matrix can be observed. It is worth underlining that the evolutions of the protein loading profiles depend on the initial WPI density. As observed for the 20 *wt*% gel, the 15 *wt*% gel shows a clearly visible protein loading maximum in the center of the gel when solvent exchange is completed. The 22.5 *wt*% gel shows a much more homogeneous protein distribution over its cross-section.

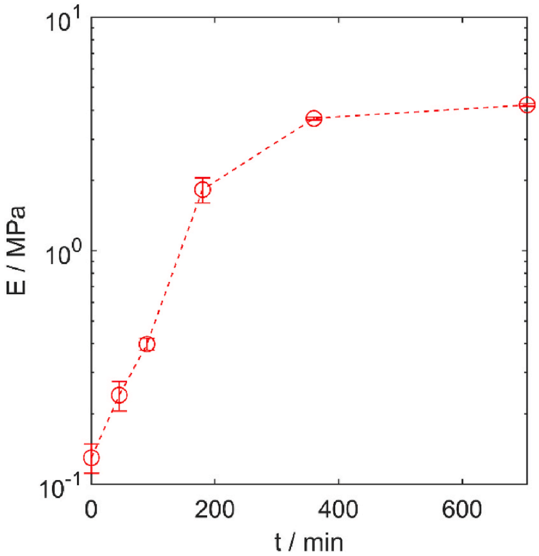

Fig. 6. Evolution of the Young's modulus of 20 *wt*% protein hydrogels during single-stage solvent exchange with pure ethanol. Note the log-scale of the y-axis.

As with the 20 *wt*% protein gel, the evolution of the gel diameter and Young's modulus have been analyzed for the 15 *wt*% and 22.5 *wt*% gels. Fig. 8 (left axis) shows the evolution of the diameter of the three different gels during solvent exchange. The three gels exhibit roughly the same shrinkage behavior with most of the shrinkage taking place during the first 90 *min* of solvent exchange. The least dense gel with a protein content of 15 *wt*% shows a faster shrinkage in the first 120 *min* compared to the denser gels. However, the final diameter for all gels is nearly the same, independent of the initial protein density of the gel. This has also been confirmed by manually measuring the diameter of each gel after solvent exchange with a slide gauge. This finding points to a nearly constant degree of shrinkage across all protein concentrations, in agreement with our previously published data compilation (Gurikov et al., 2019).

On the right axis of Fig. 8 the Young's modulus of the gels during solvent exchange is shown. All gels show an increase of the Young's modulus of at least one order of magnitude during solvent exchange with most of the gain taking place during the first 90 *min*. The hydrogels ($t = 0$ *min*) show a very strong dependence of the Young's modulus on the protein density. The initial Young's modulus of the hydrogels increases with protein concentration from 0.011 *MPa* for the 15 *wt*% gel by over one order of magnitude to 0.13 *MPa* for the 20 *wt*% gel and then again nearly doubles to 0.24 *MPa* for the 22.5 *wt*% gel. This finding is in agreement with well-known power-law dependency of the Young's modulus on the gel density (Gerlach & Arndt, 2009).

In the course of solvent exchange, all gels increase their Young's modulus with the strongest increase being observable for the 15 *wt*% gel and the least increase for the 22.5 *wt*% gel. The 15 *wt*% gel shows an increase of its Young's modulus of more than two orders of magnitude. This is in good accordance with reported literature data. The Young's modulus of a 15 *wt*% WPI gel was found to change by nearly two orders of magnitude when exchanging the water inside the pores first with acetone and afterwards with sunflower oil (Vries, Hendriks, van der Linden, & Scholten, 2015). At the end of solvent exchange, all gels show roughly the same order of magnitude of the Young's modulus within the margin of uncertainty (root mean square deviation) of the measurements. It is rather surprising that the shrinkage of the gel is not strongly dependent on the initial protein density and the Young's modulus.

An explanation for this behavior can be found when considering the kinetics of solvent exchange together with the pore liquid dependent shrinkage and mechanical stiffness. The mass transfer in a binary fluid system confined in a porous solid matrix can be explained and modelled using the effective binary diffusion coefficient. It is defined as the binary diffusion coefficient times the porosity of the solid matrix divided by its tortuosity (Dogu & Smith, 1975). Whereas the binary diffusion coefficient is a property of the fluid mixture, porosity and tortuosity are geometric properties of the porous matrix. The larger the initial protein concentration of the gel is, the smaller is its porosity. Furthermore, according to (Pisani, 2011) porosity and tortuosity for nearly all

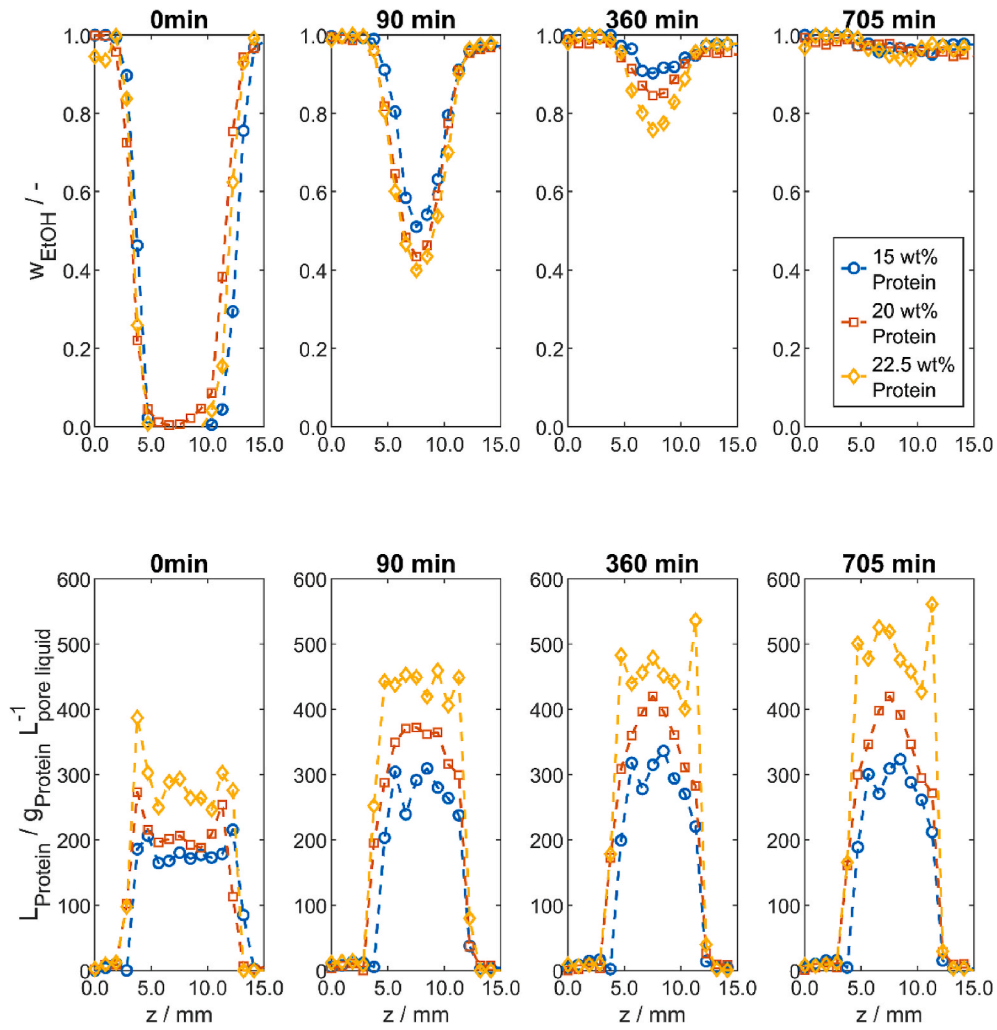

Fig. 7. Evolution of the composition profiles of pore liquid (top row) and protein loading (bottom row) of WPI gels with different protein densities during solvent exchange in pure EtOH.

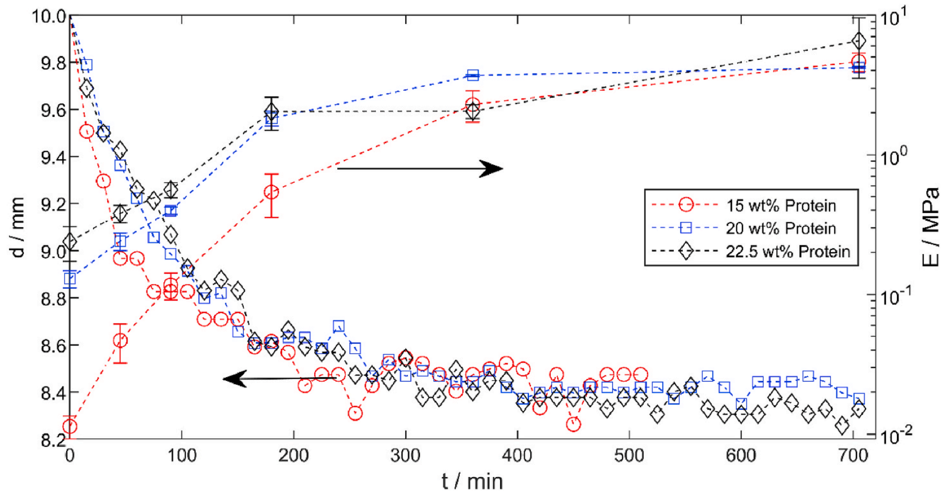

Fig. 8. Evolution of the diameter (left axis) and the elasticity modulus (right axis) of WPI hydrogels with different protein densities during solvent exchange in pure EtOH. Dotted lines are to guide the eye, arrows assign the diameter and elasticity modulus curves to the respective y-axis.

geometries and materials of practical interest feature opposing trends. It is thus concluded that the effective binary diffusion coefficients in gels with large initial protein concentration are smaller than in gels with smaller initial protein concentration. Smaller effective diffusion coefficients lead to larger radial composition gradients of the pore fluid and to longer times for completion of solvent exchange.

This theoretical consideration can be validated with the composition profiles in Fig. 7: For the time step of 90 *min*, the maximum composition gradient of the pore fluid between outer layers and the center of the gel is approximately 60 *wt*% EtOH (100 − 40 *wt*%) for the 22.5 *wt*% protein gel, while it is just 49 *wt*% EtOH (100 − 51 *wt*%) for the 15 *wt*% protein gel. This gradient between inner and outer layer gets even more pronounced with increasing time.

Higher radial pore fluid composition gradients for denser gels imply that areas with low ethanol content (in the center) coexist for a longer time with areas with high ethanol content (outer layers). The ethanol-rich mechanically stiff outer layers exhibit shrinkage and in the consequence compress the ethanol-poor and mechanically weak layers in the center of the gel, leading to a relatively high degree of shrinkage.

For the gels with lower protein content, the mechanism works vice versa: Smaller radial pore fluid composition gradients lead to a fast diffusion of ethanol into the inner layers of the gel, thereby strengthening them against further pressure due to shrinkage of the outer layers. This mechanism may explain why hydrogels with different protein content and thereby different mechanical strength show a comparable degree of shrinkage during solvent exchange.

4. Conclusions

We analyzed the one step solvent exchange of WPI hydrogels in pure ethanol using a combination of Raman spectroscopy, photography and compressive strength test. Raman spectroscopy revealed the composition profiles through the gel, conventional photography accessed the shrinkage of the central diameter of the gel and the compressive strength measurements gave new insights into shrinkage phenomena accompanying solvent exchange of protein gels.

The comparison of three gels with different protein loading showed a faster solvent exchange for the gels with lower protein density. This can be explained by the dependency of variables that characterize the pore network like pore-size-distribution, porosity and tortuosity on the protein content of the gels. Interestingly, gels showed a comparable shrinkage independently of their initial protein loading. But gels with larger protein content showed significantly higher mechanical strength as determined by the measurement of the Young's moduli of the gels. The gel shrinkage led to different radial protein density profiles: while lower density gels (15 and 20 *wt*% gels) show a rather inhomogeneous protein density profile with a compaction towards their center, the 22.5 *wt*% gel shows a much more homogeneous protein density profile. Especially when the final (aero-)gels should be used as carrier material for the well-defined release of pharmaceutically active compounds, the radial density distribution of the protein network might influence the release profile.

For all gels, most shrinkage takes place during the beginning of solvent exchange. Probably the early phase of solvent exchange increases the Young's modulus in the gel's outer regions and generates something like a rigid skeleton around inner regions, which have not yet been subject to solvent exchange. This outer rigid shell counteracts the further shrinkage of the gel. In order to describe the extraordinary change in mechanical strength, one might look at the gelation step of protein gels: With protein-based gels, during heat-induced or ethanol-assisted gelation, it is well known that there is a change from regions with alpha-helices to beta-sheet conformation (Uzun et al., 2016). Beta-sheets have a remarkably higher mechanical strength than alpha-helices. Furthermore, dominantly alpha-helical protein structures can withstand high elastic deformations at low counterforces, whereas beta-sheet structures show high mechanical stiffness with low elasticity (Buehler & Keten, 2008). The stress-strain curves show a change from linear elastic, to brittle and stiff gels. This fact further supports the argument that during the transition from hydrogel to alcogel, the proteins in the gel matrix undergo a transition from regions with alpha-helical secondary structures to beta-sheet structures. This transition and the accompanying increase in mechanical stability might be the reason for limited shrinkage of protein gels during solvent exchange. The observation that a change in the compressive strength of the gel likely stops the shrinkage of the protein matrix has consequences for predicting shrinkage during solvent exchange: A pure thermodynamic approach to describe the shrinkage of biopolymer hydrogels during solvent exchange e.g. by using Hansen solubility parameters of the solvent (Subrahmanyam et al., 2015), is probably not sufficient for describing shrinkage of WPI hydrogels in pure EtOH.

Rather, shrinkage of WPI gels during solvent exchange is a complex process governed by the kinetics of the pore fluid exchange inside the gel. Our findings suggest that solvent exchange, shrinkage and compressive strength (the latter two strongly dependent on the pore fluid composition) have competing effects on the final shape.

Acknowledgement

The authors gratefully acknowledge financial support for parts of this work through the projects BR 3766/19–1 and GU 1842/3-1 by the German Research Foundation (Deutsche Forschungsgemeinschaft – DFG).

Appendix A. Computation of composition from Raman raw spectra

Spectra processing

In order to extract information of the mixture composition from the raw spectra, the spectra are first baseline corrected to remove fluorescence interference. There are two main challenges involving baseline correction: First, the shape of the background is a strong function of the position of the measurement volume. Outside the gel, the spectra basically appear like the pure Raman spectra of water-EtOH with very little background. Inside the gel, depending on the actual protein density one can observe strong background signals (c.f. Fig. A- 1) especially in the region from 1000 to 2000 cm^{-1}. The second challenge is the different peak shape. While the protein peak is rather sharp and defined, the water band is broad. The changing intensity of the background, together with the different peak shapes make automated background correction quite challenging for standard techniques like polynomial background correction, but also for advanced methods like asymmetric least squares.

A function of the basic form 1/x proved to give a good model for the background for spectra inside and outside the gel.

$$y = a(x-b)^{c} + d \tag{A- 1}$$

The parameters a, b, c, d in equation (A- 1) are optimized for the best fit of the background. As grid points the regions from $1464 - 1526\ \mathrm{cm}^{-1}$, $1809 - 2394\ \mathrm{cm}^{-1}$ and 3661 to $3926\ \mathrm{cm}^{-1}$ where chosen. The so derived background function was then subtracted from the raw spectra. Fig. A- 1 shows the original spectra taken at a position inside the gel together with the regions that serve as grid for the fit and the fitted background.

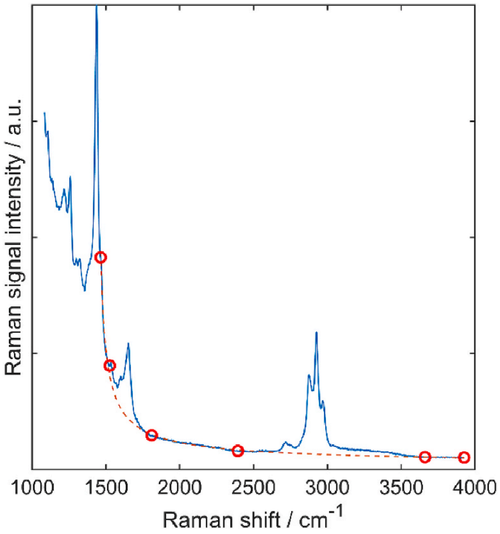

Fig. A -1. Example of a Raman spectrum inside the gel during solvent exchange with fitted background function (dashed line) and the borders of the areas used for fitting the background function (circles).

The baseline corrected spectra are then integrated from 1543 to 1711 cm^{-1} for the intensity of the protein signal $I_{Protein}$, from 2662 to 2757 cm^{-1} for EtOH signal intensity I_{EtOH} and from 3316 to 3549 cm^{-1} for water signal intensity I_{H2O}.

Calibration

From the three Raman signal intensities assignable to the three different compounds the three intensity ratios of equation (A- 2)-(A- 4) can be calculated.

$$r_{EtOH/H2O} = \frac{I_{EtOH}}{I_{H2O}} \tag{A- 2}$$

$$r_{Protein/H2O} = \frac{I_{Protein}}{I_{H2O}} \tag{A- 3}$$

$$r_{Protein/EtOH} = \frac{I_{Protein}}{I_{EtOH}} \tag{A- 4}$$

In order to link the intensity ratio in the spectra to the binary molar ratio of two substances, calibration samples with known binary molar ratios are measured and the resulting molar ratio is plotted over the intensity ratio. Fig. A- 2shows this for the binary mixture of EtOH and water.

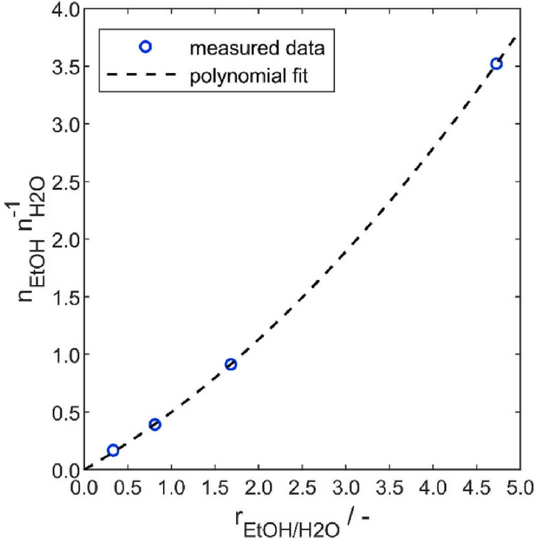

Fig. A -2. Calibrated molar Ratio EtOH/Water as a function of the Intensity ratio $r_{EtOH/H2O}$.

For this calibration samples with 10, 50, 70, 90 *wt*% EtOH were measured. To account for minor influences from the protein gel matrix, the spectra were measured inside a 20 *wt*% protein gel that was immersed in an excess amount of the respective water-EtOH mixture for 48 *h*. This ensured the composition of the pore liquid at every point in the gel is the same as in the surrounding liquid outside the gel. The resulting spectra from the 17 measurement locations (inside and outside the gel) are then averaged and the resulting intensity ratios are fitted to the polynomial of second order in equation (A- 5). The fit resulted in an r^2 value of 1.00.

$$\frac{n_{EtOH}}{n_{H2O}} = a_1 \cdot r_{EtOH/H2O}{}^2 + b_1 \cdot r_{EtOH/H2O} \tag{A- 5}$$

For a ternary system as in this case with water, EtOH and protein it would be sufficient to set-up only two calibration functions. With the one shown above for water-EtOH, a second for e.g. protein-water would be enough to calculate the fraction of each single compound in the ternary mixture. However, this does not lead to accurate measurements due to a lack of ethanol inside the gel at the beginning of solvent exchange and, vice versa, that there is virtually no water to be found after completed solvent exchange. To make the prediction of the protein content more stable, two independent protein mole fractions $x_{P\frac{Protein}{water}}$ and $x_{P\frac{Protein}{EtOH}}$ are calculated by using both intensity ratios $r_{Protein/Water}$ and $r_{Protein/EtOH}$. These two mole fractions are then weighted with the binary weight fraction of ethanol to get a combined mole fraction of protein x_{P_mix} that is more independent of the water/EtHO ratio.

$$x_{P\_mix} = (1 - x_{EtOH}) \cdot x_{P\left(\frac{Protein}{H2O}\right)} + x_{EtOH} \cdot x_{P\frac{Protein}{EtOH}} \tag{A- 6}$$

The calibration functions for protein-water and protein-EtOH cannot be produced straight forward. First, the protein powder is nearly completely insoluble in EtOH. Second, it is known from literature, that the spectra of protein in aqueous solution are subject to change during rehydration and thermal denaturation. This means it is not suitable to just measure a solution of protein in aqueous solution for calibration.

To overcome this issue, a different calibration strategy was employed. It was assumed, that the shapes of the calibration curves for protein-water and protein-EtOH can also be described by a polynomial of second order as it was the case for EtOH-water.

$$\frac{n_{Protein}}{n_{water}} = a_2 \cdot r_{Protein/H2O}{}^2 + b_2 \cdot r_{Protein/H2O} \tag{A- 7}$$

$$\frac{n_{Protein}}{n_{EtOH}} = a_3 \cdot r_{Protein/EtOH}{}^2 + b_3 \cdot r_{Protein/EtOH} \tag{A- 8}$$

For one run of solvent exchange, it is known that the mass of the protein gel matrix stays constant. Assuming shrinkage of the gel in axial dimension is much less pronounced than in radial dimension, the amount of protein χ in one radial slice of the gel cylinder with the radius R and height h stays constant during solvent exchange.

$$\frac{m_{Protein}}{h} = \chi = \int_0^R L_{Protein}(r)\, 2\pi r\, dr = const \tag{A- 9}$$

The value of χ for a specific gel can be calculated from the initial gel diameter and the original protein concentration during gelation. This results in values of $0.0138\, g\, mm^{-1}$, $0.0196\, g\, mm^{-1}$ and $0.0228\, g\, mm^{-1}$ for gels with $15\, wt\%$, $20\, wt\%$ and $22.5\, wt\%$ original protein content in the hydrogel respectively. In order to calculate the parameters a_2, b_2, a_3, b_3 in equations (A- 7) and (A- 8), solvent exchange of 15, 20, $22.5\, wt\%$ protein hydrogels in pure EtOH were measured. For every point in time during solvent exchange, χ was calculated. The parameters of equations (A- 7) and (A- 8) where then optimized so that the value of χ stays the predefined constant value for each protein concentration. The value of χ during solvent exchange for three different gels is shown in Fig. A- 3. The shape of each curve shows approximately the predicted shape of a horizontal line with deviation of the slopes in positive and negative direction. The nearly closed mass balance of the protein matrix material over the whole measurement volume during one complete run of solvent exchange is a strong indication of the suitability of the applied Raman measurement technique together with the applied spectra processing routine for measuring protein density distribution inside gels in changing solvent environment.

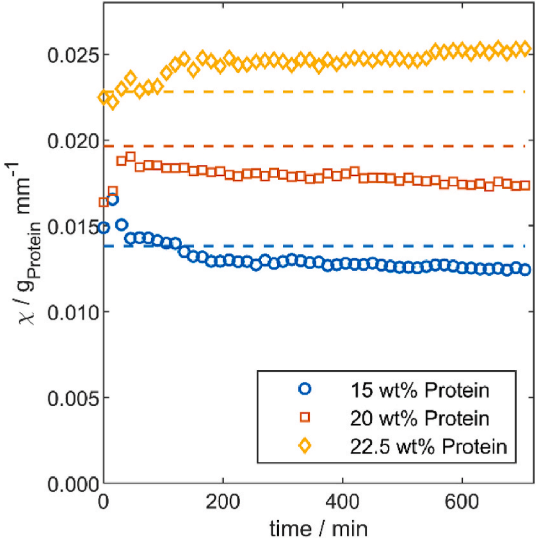

Fig. A -3. Temporal evolution of the locally summed protein loading of three different protein gels during solvent exchange in pure EtOH. Dashed lines show expected values of χ for each gel.

The parameters from this fit together with the parameters for the EtOH/water calibration are shown in Table A- 1.

Table A- 1
Parameters for the calibration functions of EtOH und Protein

	a_i	b_i
$r_{EtOH/H20}$	0.06607	0.43250
$r_{Protein/H2O}$	0.0000010000	0.02836
$r_{Protein/EtOH}$	0.0000010000	0.08408

Appendix B. Reproducibility of the composition profiles

All composition profiles shown in this work were the results from single experiments. The reason for not using average values derived from several identical experiments is due to the two major challenges in combining and averaging composition profiles from independent experiments: (i) It is difficult to place two gels on the exact same position in the cuvette during solvent exchange. (ii) Shrinkage can lead to movement of the gels, which further shifts position of the gels on the local axis. These reasons make a spatial shifting of the individual concentration profiles to a common reference point inevitable before averaging concentration profiles of individual experiments. The limited spatial resolution of the Raman measurements requires to interpolate the composition profiles for shifts that are not by coincident multiples of the spatial resolution. Especially when high concentration gradients are present, the interpolation needed to shift the concentration profiles of several independent experiments likely introduces relevant deviations.

Despite the arguments mentioned above, three completely independent solvent exchange experiments of 20 *wt*% WPI hydrogels in pure EtOH have been carried out to get an orientating impression of the reproducibility. Concentration profiles were shifted on the spatial axis to reach minimum deviation between the three experiments. The resulting averaged composition profiles of the three experiments are shown in Fig. B- 1.

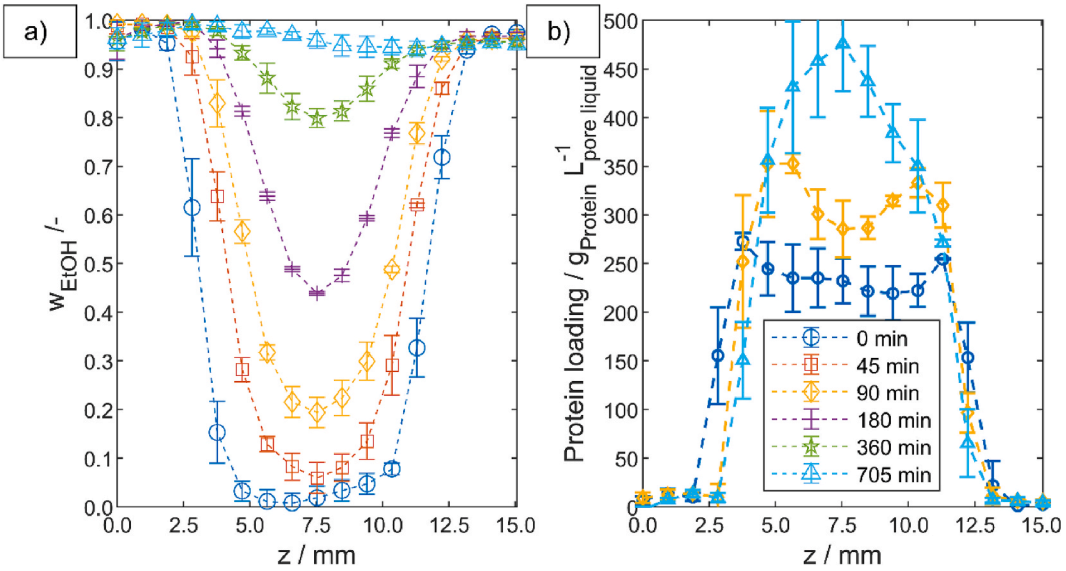

Fig. B -1. Averaged composition profiles of pore liquid (a) and protein loading (b) during solvent exchange of 20 wt% WPI hydrogels in pure EtOH. Only three instances in time are shown in b) for clarity. Error bars represent the calculated standard deviation.

As can be seen in the averaged ethanol profiles in Figure B- 1 a), averaged profiles are very similar to the curves of the single experiment shown in Fig. 3 b). The calculated error bars do not cross the lines of adjacent measurements times. However, as discussed above, error bars are small where small gradients are observed and large were the gradients have large values. The size of the error bars at positions with large gradients however is very likely caused by an insufficient overlay of the single composition profiles. This can also be observed with the protein loading profiles in Figure B- 1 b): Error bars are largest, where the protein loading curves show their largest gradients, that is at the boundaries of the gel. However, error bars indicate that the development of the protein loading profile from an almost homogeneous protein loading over the cross-section at $t = 0$ min towards a densification of the protein density in the middle of the gel at the end of solvent exchange ($t = 705\ min$) can clearly be derived from the Raman measurements.

Author statement

Martin P. Dirauf: Methodology, Investigation, Software, Writing – Original Draft, Visualization.
Anja Hajnal: Writing – Review & Editing.
Pavel Gurikov: Writing – Review & Editing, Funding acquisition.
Andreas S. Braeuer: Conceptualization, Methodology, Writing – Review & Editing, Supervision, Project administration, Funding acquisition.

References

Betz, M., García-González, C. A., Subrahmanyam, R. P., Smirnova, I., & Kulozik, U. (2012). Preparation of novel whey protein-based aerogels as drug carriers for life science applications. *The Journal of Supercritical Fluids, 72*, 111–119. https://doi.org/10.1016/j.supflu.2012.08.019

Buck, M. (1998). Trifluoroethanol and colleagues: Cosolvents come of age. Recent studies with peptides and proteins. *Quarterly Reviews of Biophysics, 31*(3), 297–355. https://doi.org/10.1017/s003358359800345x

Buehler, M. J., & Keten, S. (2008). Elasticity, strength and resilience: A comparative study on mechanical signatures of α-Helix, β-sheet and tropocollagen domains. *Nano Research, 1*(1), 63–71. https://doi.org/10.1007/s12274-008-8006-7

Chen, J., Dickinson, E., & Edwards, M. (1999). Rheology OF acid-induced sodium caseinate stabilized emulsion gels. *Journal of Texture Studies, 30*(4), 377–396. https://doi.org/10.1111/j.1745-4603.1999.tb00226.x

Dogu, G., & Smith, J. M. (1975). A dynamic method for catalyst diffusivities. *AIChE Journal, 21*(1), 58–61. https://doi.org/10.1002/aic.690210106

El-Naggar, M. E., Othman, S. I., Allam, A. A., & Morsy, O. M. (2020). Synthesis, drying process and medical application of polysaccharide-based aerogels. *International Journal of Biological Macromolecules, 145*, 1115–1128. https://doi.org/10.1016/j.ijbiomac.2019.10.037

Fricke, J., & Tillotson, T. (1997). Aerogels: Production, characterization, and applications. *Thin Solid Films, 297*(1–2), 212–223. https://doi.org/10.1016/S0040-6090(96)09441-2

García-González, C. A., Alnaief, M., & Smirnova, I. (2011). Polysaccharide-based aerogels—promising biodegradable carriers for drug delivery systems. *Carbohydrate Polymers, 86*(4), 1425–1438. https://doi.org/10.1016/j.carbpol.2011.06.066

García-González, C. A., Camino-Rey, M. C., Alnaief, M., Zetzl, C., & Smirnova, I. (2012). Supercritical drying of aerogels using CO2: Effect of extraction time on the end material textural properties. *The Journal of Supercritical Fluids, 66*, 297–306. https://doi.org/10.1016/j.supflu.2012.02.026

Gerlach, G., & Arndt, K.-F. (2009). *Hydrogel sensors and actuators: Engineering and Technology (Online-ausg). SpringerLink* (Vol. 6). Berlin, Heidelberg: Springer e-Books. Springer-Verlag Berlin Heidelberg.

Grolier, J.-P. E., & Wilhelm, E. (1981). Excess volumes and excess heat capacities of water + ethanol at 298.15 K. *Fluid Phase Equilibria, 6*(3–4), 283–287. https://doi.org/10.1016/0378-3812(81)85011-X

Groult, S., & Budtova, T. (2018). Tuning structure and properties of pectin aerogels. *European Polymer Journal, 108*, 250–261. https://doi.org/10.1016/j.eurpolymj.2018.08.048

Gurikov, P., Raman, S. P., Weinrich, D., Fricke, M., & Smirnova, I. (2015). A novel approach to alginate aerogels: Carbon dioxide induced gelation. *RSC Advances, 5* (11), 7812–7818. https://doi.org/10.1039/C4RA14653K

Gurikov, P., R, S. P., Griffin, J. S., Steiner, S. A., & Smirnova, I. (2019). 110th anniversary: Solvent exchange in the processing of biopolymer aerogels: Current status and open questions. *Industrial & Engineering Chemistry Research, 58*(40), 18590–18600. https://doi.org/10.1021/acs.iecr.9b02967

Heinemann, M., Meinberg, H., B&uuml, J., chs, H.-J.&uuml, Ko&szlig, rgen, & Ansorge-Schumacher, M. B. (2004). Method for quantitative determination of spatial polymer distribution in alginate beads using Raman spectroscopy. *Applied Spectroscopy, 59*(3), 280–284.

Hongsprabhas, P., & Barbut, S. (1997). Protein and salt effects on Ca2+-induced cold gelation of whey protein isolate. *Journal of Food Science, 62*(2), 382–385. https://doi.org/10.1111/j.1365-2621.1997.tb04006.x

Kleemann, C., Selmer, I., Smirnova, I., & Kulozik, U. (2018). Tailor made protein based aerogel particles from egg white protein, whey protein isolate and sodium caseinate: Influence of the preceding hydrogel characteristics. *Food Hydrocolloids, 83*, 365–374. https://doi.org/10.1016/j.foodhyd.2018.05.021

Maleki, H., Durães, L., García-González, C. A., Del Gaudio, P., Portugal, A., & Mahmoudi, M. (2016). Synthesis and biomedical applications of aerogels: Possibilities and challenges. *Advances in Colloid and Interface Science, 236*, 1–27. https://doi.org/10.1016/j.cis.2016.05.011

Marin, M. A., Mallepally, R. R., & McHugh, M. A. (2014). Silk fibroin aerogels for drug delivery applications. *The Journal of Supercritical Fluids, 91*, 84–89. https://doi.org/10.1016/j.supflu.2014.04.014

Mehling, T., Smirnova, I., Guenther, U., & Neubert, R. H. H. (2009). Polysaccharide-based aerogels as drug carriers. *Journal of Non-crystalline Solids, 355*(50–51), 2472–2479. https://doi.org/10.1016/j.jnoncrysol.2009.08.038

Naddaf, A. A., & Bart, H. J. (2011). Raman spectroscopy: Mutual diffusion coefficient in hydrogels. *Defect and Diffusion Forum, 312–315*, 193–198. https://doi.org/10.4028/www.scientific.net/DDF.312-315.193.

Nonaka, M., Li-Chan, E., & Nakai, S. (1993). Raman spectroscopic study of thermally induced gelation of whey proteins. *Journal of Agricultural and Food Chemistry, 41*(8), 1176–1181. https://doi.org/10.1021/jf00032a002

Pisani, L. (2011). Simple expression for the tortuosity of porous media. *Transport in Porous Media, 88*(2), 193–203. https://doi.org/10.1007/s11242-011-9734-9

Quignard, F., Valentin, R., & Di Renzo, F. (2008). Aerogel materials from marine polysaccharides. *New Journal of Chemistry, 32*(8), 1300. https://doi.org/10.1039/b808218a

Quiño, J., Ruehl, M., Klima, T., Ruiz, F., Will, S., & Braeuer, A. (2016). Supercritical drying of aerogel: In situ analysis of concentration profiles inside the gel and derivation of the effective binary diffusion coefficient using Raman spectroscopy. *The Journal of Supercritical Fluids, 108*, 1–12. https://doi.org/10.1016/j.supflu.2015.10.011

Selmer, I., Kleemann, C., Kulozik, U., Heinrich, S., & Smirnova, I. (2015). Development of egg white protein aerogels as new matrix material for microencapsulation in food. *The Journal of Supercritical Fluids, 106*, 42–49. https://doi.org/10.1016/j.supflu.2015.05.023

Soorbaghi, F. P., Isanejad, M., Salatin, S., Ghorbani, M., Jafari, S., & Derakhshankhah, H. (2019). Bioaerogels: Synthesis approaches, cellular uptake, and the biomedical applications. *Biomedicine & Pharmacotherapy = Biomedecine & Pharmacotherapie, 111*, 964–975. https://doi.org/10.1016/j.biopha.2019.01.014

Stergar, J., & Maver, U. (2016). Review of aerogel-based materials in biomedical applications. *Journal of Sol-Gel Science and Technology, 77*(3), 738–752. https://doi.org/10.1007/s10971-016-3968-5

Subrahmanyam, R., Gurikov, P., Dieringer, P., Sun, M., & Smirnova, I. (2015). On the road to biopolymer aerogels-dealing with the solvent. *Gels (Basel, Switzerland), 1*(2), 291–313. https://doi.org/10.3390/gels1020291

Uzun, S., Kim, H., Leal, C., & Padua, G. W. (2016). Ethanol-induced whey protein gels as carriers for lutein droplets. *Food Hydrocolloids, 61*, 426–432. https://doi.org/10.1016/j.foodhyd.2016.05.013

Van Kleef, F. S. (1986). Thermally induced protein gelation: Gelation and rheological characterization of highly concentrated ovalbumin and soybean protein gels. *Biopolymers, 25*(1), 31–59. https://doi.org/10.1002/bip.360250105

Vries, A. de, Hendriks, J., van der Linden, E., & Scholten, E. (2015). Protein oleogels from protein hydrogels via a stepwise solvent exchange route. *Langmuir : The ACS Journal of Surfaces and Colloids, 31*(51), 13850–13859. https://doi.org/10.1021/acs.langmuir.5b03993

Wolz, M., & Kulozik, U. (2015). Thermal denaturation kinetics of whey proteins at high protein concentrations. *International Dairy Journal, 49*, 95–101. https://doi.org/10.1016/j.idairyj.2015.05.008

Zhu, F. (2019). Starch based aerogels: Production, properties and applications. *Trends in Food Science & Technology, 89*, 1–10. https://doi.org/10.1016/j.tifs.2019.05.001